Soft Matter

Accepted Manuscript

This is an *Accepted Manuscript*, which has been through the Royal Society of Chemistry peer review process and has been accepted for publication.

Accepted Manuscripts are published online shortly after acceptance, before technical editing, formatting and proof reading. Using this free service, authors can make their results available to the community, in citable form, before we publish the edited article. We will replace this *Accepted Manuscript* with the edited and formatted *Advance Article* as soon as it is available.

You can find more information about *Accepted Manuscripts* in the Information for Authors.

Please note that technical editing may introduce minor changes to the text and/or graphics, which may alter content. The journal's standard Terms & Conditions and the Ethical guidelines still apply. In no event shall the Royal Society of Chemistry be held responsible for any errors or omissions in this *Accepted Manuscript* or any consequences arising from the use of any information it contains.

ROYAL SOCIETY OF CHEMISTRY

www.rsc.org/softmatter

Kinetic attractor phase diagrams of active nematic suspensions: the dilute regime

M. Gregory Forest
Departments of Mathematics, Biomedical Engineering,
and Applied Physical Sciences
University of North Carolina at Chapel Hill
Chapel Hill, NC 27599

Qi Wang
Department of Mathematics
University of South Carolina
Columbia, SC 29208
and
Beijing Computational Science Research Center
Beijing, China 100084

Ruhai Zhou
Department of Mathematics and Statistics
Old Dominion University
Norfolk, VA 23529

July 5, 2015

Abstract

Large-scale simulations by the authors [10] of the kinetic-hydrodynamic equations for active polar nematics revealed a variety of spatio-temporal attractors, including steady and unsteady, banded (1d) and cellular (2d) spatial patterns. These particle scale activation-induced attractors arise at *dilute* nanorod volume fractions where the passive equilibrium phase is isotropic, whereas all previous model simulations have focused on the semi-dilute, nematic equilibrium regime and mostly on low-moment orientation tensor and polarity vector models [13, 15, 24, 25, 26, 28, 34, 35, 36]. Here we extend our previous results to complete attractor phase diagrams for active nematics, with and without an explicit polar potential, to map out novel spatial and dynamic transitions, and to identify some new attractors, over the parameter space of dilute nanorod volume fraction and nanorod activation strength.

The particle-scale activation parameter corresponds experimentally to a tunable force dipole strength (so-called pushers with propulsion from the rod tail) generated by active rod macromolecules, e.g., catalysis with the solvent phase [30, 33, 47], ATP-induced propulsion [19], or light-activated propulsion [32]. The simulations allow 2d spatial variations in all flow and orientational variables and full spherical orientational degrees of freedom; the attractors correspond to numerical integration of a coupled system of 125 nonlinear PDEs in 2d plus time. The phase diagrams with and without the polar interaction potential are remarkably similar, implying that polar interactions among the rodlike particles are not essential to long-range spatial and temporal correlations in flow, polarity, and nematic order. As a general rule, above a threshold, low volume fractions induce 1d banded patterns, whereas higher yet still dilute volume fractions yield 2d patterns. Again as a general rule, varying activation strength at fixed volume fraction induces novel dynamic transitions. First, stationary patterns saturate the instability of the isotropic state, consisting of discrete 1d banded or 2d cellular patterns depending on nanorod volume fraction. Increasing activation strength further induces a sequence of attractor bifurcations, including oscillations superimposed on the 1d and 2d stationary patterns, a uniform translational motion of 1d and 2d oscillating patterns, and periodic switching between 1d and 2d patterns. These results imply that active macromolecular suspensions are capable of long-range spatial and dynamic organization *at isotropic equilibrium concentrations*, provided particle-scale activation is sufficiently strong.

1 Kinetic-hydrodynamic model [10]

A kinetic model was developed in [10] for active dispersions of rod-like macromolecules of relatively large aspect ratio. Our approach was to start from the highly developed and experimentally benchmarked kinetic theory for flowing passive nematic polymers, owing to contributions of Doi, Edwards [3], Hess[16], Marrucci and Greco [27]. We recall the lesson learned from passive nematic polymer simulations: low-moment closures of Landau-deGennes type capture qualitative features of both equilibrium and non-equilibrium, steady and unsteady, attractors in a variety of geometries and forcing conditions. However, every such closure model fails to have quantitative accuracy in comparison with the kinetic theory, and furthermore fails to get the correct transitions (bifurcations) between attractors as forcing conditions, rod concentrations, or rod aspect ratios are varied [6, 7, 8, 9]. The inaccuracies due to closure are only removed by going to a sufficiently high expansion in spherical harmonics for the orientational probability distribution function of the rodlike particle ensemble. Furthermore, restriction to planar rods, i.e., to a Fourier series for unit-length rods on the circle, instead of three-dimensional rods on the sphere and spherical harmonic expansions, completely misses many of the attractors and phase transitions of nematic polymers in shear-dominated flows. The remarkable kayaking limit cycles [22] that permeate shear cells [48] and driven cavities [49], are only possible on the sphere. In any future modeling exploration of active nematics in deformable vesicles, for example, shear-induced behavior at vesicle walls (cf. sheared passive nematic droplet phenomena [5]) will interact with the ”free space” phenomena explored thus far for active nematics with periodic boundary conditions. These lessons and sights on future applications are our motivation to develop a full orientation space, full kinetic theory for active nematics, and rigorous, comprehensive simulations thereof.

From this rigorous foundation for passive nematics, in [10] we incorporated the statistical physics of particle-scale activation, including a swimming speed of the active particles, a polar interaction potential in addition to the Maier-Saupe nematic potential, and activation-induced extra stress contributions. In this way, our previous numerical algorithms for passive nematic polymer hydrodynamics [6, 7, 8, 9] could be generalized with only a couple tedious but straightforward modifications. First, the swimming velocity and associated force dipole of the rod macromolecules induces polarity of the suspension, with or without a polar potential. The polarity variable is the first moment of the rod number density distribution function, so that all odd spherical harmonics of the orientational distribution function had to be added to previous expansions in even spherical harmonics of nematic polymers. The polarity of active nematics translates in any truncated spherical harmonic expansion to approximately doubling of the size of the system: from 65 real degrees of freedom for apolar nematics to 121 real degrees of freedom for polar nematics. Thus the evolutionary system of nonlinear partial differential equations (PDEs) in two space dimensions

expands from 65 + 4 (three momentum equations for the flow variables and a pressure equation) to 121 + 4, or 125. Second, instead of a confined domain of passive nematics with moving wall and no-slip boundary conditions, the typical active suspension studies impose periodic boundary conditions in both space dimensions. We point the reader to our earlier paper [10] for these details, and furthermore to recent research and review articles [26, 24, 39, 40] that give a broad motivation and overview of the experimental and modeling literature on active nematics and broader active "swimmer" suspensions. These articles also provide proper citations to the seminal literature on active suspensions.

The essential details of our model derived in [10] are recalled below, with tunable molecular features that distinguish among possible synthetic materials (e.g., catalytic nanorod dispersions [30, 47, 33] or microtubules in ATP-rich fluids [19] and their self-organized spatio-temporal behavior). *Our goal here is to extend the illustrative numerical results in [10] for active polar nematics to complete attractor phase diagrams with and without the polar interaction potential.* These results require detailed, long time, large scale, numerical simulations of the active kinetic-hydrodynamic system. Our approach here, as in [10], is not to introduce low-moment closures, but rather to go sufficiently high in the spherical harmonic expansion (121 real degrees of freedom) in the particle orientational configuration space so that we remove the influence of closure approximations. This comes with a significant computational expense, yet we believe the results justify the cost. In particular, in [10] and the results presented here, we find that active nematics of sufficient dipole strength exhibit long-range spatial correlations and unsteady behavior even at dilute concentrations where the passive dispersion is isotropic. Intuitively, sufficiently strong nanorod swimmers obviate the need for a stronger nematic ordering potential. Previously reported results of active nematic spatio-temporal states with Landau-deGennes type, low order truncated models, focus on nematic equilibrium concentrations.

The dimensionless equation for the nanorod number density function (NDF) $f(\mathbf{m},\mathbf{x},t)$ with constant translational diffusion coefficient D_s and rotational diffusion coefficient D_r is given by

$$\frac{\partial f}{\partial t}+\nabla\cdot((\mathbf{v}+U_0\mathbf{m})f)=D_s\nabla\cdot(\nabla f+f\nabla U)+D_r f_0^{-2}\mathcal{R}\cdot(\mathcal{R}f+f\mathcal{R}U)-\mathcal{R}\cdot(\mathbf{m}\times\dot{\mathbf{m}}f), \qquad (1)$$

where U_0 is the rod self-propulsion speed (which is set to unity throughout the paper), $\mathbf{m}$ is the unit vector representing the axis of symmetry of the rodlike macromolecule, ∇ represents the spatial gradient operator, and $\mathcal{R}=\mathbf{m}\times\frac{\partial}{\partial\mathbf{m}}$ is the rotational gradient operator (see Doi and Edwards [3]). The intermolecular potential U is given as follows

$$U=N_1 f_0-\alpha\mathbf{n}\cdot\mathbf{m}-\frac{3N}{2}\mathbf{M}:\mathbf{mm}, \qquad (2)$$

with N_1, α, and N representing the strengths of the potentials for spatial inhomogeneity, polarity and nematic order, respectively. The nematic parameter N is proportional to the rod macromolecular

volume fraction (or concentration); for passive nematics, the isotropic-nematic phase diagram [7] reveals a stable isotropic equilibrium for all $N < 5$, which is the range explored here. Likewise, the strength of polar interaction potential α is also proportional to the rod macromolecular volume fraction. The local concentration f_0, the polarity director $\mathbf{n}$ and the second moment orientation tensor $\mathbf{M}$ are defined as the zeroth, first and second moment of $f(\mathbf{m},\mathbf{x},t)$ on the unit sphere, respectively:

$$f_0(\mathbf{x},t) = \langle 1 \rangle = \int_{||\mathbf{m}||=1} f(\mathbf{m},\mathbf{x},t)\, d\mathbf{m}, \tag{3}$$

$$\mathbf{n}(\mathbf{x},t) = \langle \mathbf{m} \rangle = \int_{||\mathbf{m}||=1} \mathbf{m} f(\mathbf{m},\mathbf{x},t)\, d\mathbf{m}, \tag{4}$$

$$\mathbf{M}(\mathbf{x},t) = \langle \mathbf{mm} \rangle = \int_{||\mathbf{m}||=1} \mathbf{mm} f(\mathbf{m},\mathbf{x},t)\, d\mathbf{m}. \tag{5}$$

Note that the rotational diffusion term is normalized by f_0^{-2} [3], which is the only modification from the model in [10]. The Jeffery orbit $\dot{\mathbf{m}}$ in (1) is

$$\dot{\mathbf{m}} = \mathbf{W}\cdot\mathbf{m} + a[\mathbf{D}\cdot\mathbf{m} - \mathbf{D} : \mathbf{mmm}], \tag{6}$$

where $0 \le a \le 1$ is a geometric particle parameter for rods, $a = (r^2-1)/(r^2+1)$, with r the particle aspect ratio, and $\mathbf{D}, \mathbf{W}$ are the symmetric and anti-symmetric parts of the velocity gradient tensor. Equation (1) describes the transport of the number density function. Marchetti *et al.* have derived a similar kinetic equation for polar active rods in [2] while Shelley and Saintillan derived another variant of the kinetic theory for suspensions of self-propelled particles [36, 34, 35]. Aside from these studies, all other simulations of active nematics have studied low moment closure models of the kinetic equation, and the rods have been restricted to planar.

To close the system in the hydrodynamic kinetic theory, the Smoluchowski equation (1) is coupled to the incompressible Navier-Stokes equations

$$\frac{d\mathbf{v}}{dt} + (\mathbf{v}\cdot\nabla)\mathbf{v} = \nabla\cdot(-p\mathbf{I} + \tau_p + \tau_a), \qquad \nabla\cdot\mathbf{v} = 0. \tag{7}$$

Many authors assume zero Reynolds number and replace the Navier-Stokes equations by the Stokes equations. However, a significant body of work has studied $O(1)$ Reynolds numbers [14, 39] as we have in [10] and the present paper. The constitutive equations for the passive nematic stress τ_p and the active stress τ_a are

$$\begin{aligned} \tau_p &= 2Re^{-1}\mathbf{D} + G[\mathbf{M} - \tfrac{1}{3}f_0\mathbf{I} - N\mathbf{M}^2 + N\mathbf{M} : \langle \mathbf{mmmm} \rangle] \\ &\quad -\tfrac{1}{6}\alpha_0 G[2\mathbf{nn} - (\langle \mathbf{mmm} \rangle \cdot \mathbf{n} + \mathbf{n}\cdot\langle \mathbf{mmm} \rangle)] + Re_2^{-1}[\mathbf{D}\cdot\mathbf{M} + \mathbf{M}\cdot\mathbf{D}] + Re_3^{-1}\langle \mathbf{mmmm} \rangle : \mathbf{D}, \\ \tau_a &= G\zeta_a(\mathbf{M} - \tfrac{1}{3}f_0\mathbf{I}), \end{aligned} \tag{8}$$

where $\langle \mathbf{mmm} \rangle$ and $\langle \mathbf{mmmm} \rangle$ are third and fourth moments of f, the parameters Re, Re_2, Re_3 are Reynolds numbers for solvent and particle-solvent interactions, G is the anisotropic stress coefficient (the entropic stored stress, or zero frequency elastic modulus, normalized by inertial stress),

α_0 tunes the stored stress due to polarity (induced or primary), and ζ_a is the particle activation parameter that tunes the strength of the force dipole. A detailed choice of characteristic length, time, and stress scales that yield the values of all dimensionless parameters is given in our earlier paper [10], including an order one Reynolds number.

2 Phase diagrams of polar active nematic suspensions with and without the polar interaction potential

We solve the coupled system (1)–(8) in a normalized unit square physical domain with spatially periodic boundary conditions. The numerical method is described in [10], where we use a Galerkin spectral method with 121 spherical harmonic basis functions resulting in 125 partial differential equations for the Fourier coefficients of the number density function, the hydrostatic pressure and the three velocity components. The initial state of the NDF is a randomly perturbed isotropic state, while the flow is quiescent initially. Several dilute concentrations, all corresponding to a stable isotropic equilibrium for the Doi-Hess-Smoluchowski kinetic equation [6, 7, 8, 9], are explored: $0.5 < N < 3.5$ in increments of 0.5. For each N, we run long-time simulations for a range of activation parameter values $\zeta_a < 0$ (pushers), thereby compiling long-time attractors across the (N, ζ_a) base domain. We sample across ζ_a with sufficient detail to identify attractor phase transitions, and these phase boundaries are drawn in Figure 1 (polar active nematics without the polar interaction potential) and Figure 8 (polar active nematics with the polar interaction potential). We note that most simulations are run out to 500 non-dimensional time units (6.25×10^5 steps) , which corresponds to an experimental clock time of $2250s$ or about 37 minutes (for a typical nanorod with length ranging from 5 to $300nm$, the characteristic timescale of rotational relaxation is around $t_0 = 4.5s$ [10]). In some cases, the transients persist out to 500 time units, in which case we double the run time to be reasonably sure of convergence to a quasi-stationary asymptotic state. To be completely forthcoming, it is quite possible that these apparent stationary states are long-lived transients, but the same is true of physical experiments. The boundaries between attractor domains are resolved within .1 increments of each parameter on a relatively coarse grid, Figures 1 and 8, and then we simply connect the dots to approximate the boundaries corresponding to attractor bifurcations. We have not yet attempted to classify the precise nature of these high-dimensional bifurcations, e.g., using sophisticated continuation software such as AUTO [4] or XPPAUT [1]. We also cannot rule out hysteresis at these phase transition boundaries, but the expense to explore this across the phase diagram is prohibitive. Thiese finer resolution issues are where low-dimensional moment closures can prove useful, although we caution that several attractors reported here have not been observed in low-moment closures.

The base parameter values used to produce the phase diagrams in Figure 1 and 8 are $D_s =$

$0.02, De = 20, Re = Re_2 = Re_3 = 5, G = 4$, so that we can make direct contact with the results reported in [10] for active polar nematics, and place those attractors within the phase diagram. We begin with the phase diagram without the polar interaction potential, i.e., where polarity is induced by the force dipole of the nanorod swimmers, and then turn to the polar phase diagram with the polar interaction potential (not studied in [10]).

2.1 Active nematic suspensions with induced polarity

Figure 1 shows the phase diagram for polar active nematics without the polar interaction potential (the polar strength coefficient $\alpha = 0$ in (2) and the polar stress constant $\alpha_0 = 0$ in (8)). Shorthand labels for the various spatio-temporal structures are given in Table 1 with their detailed descriptions below.

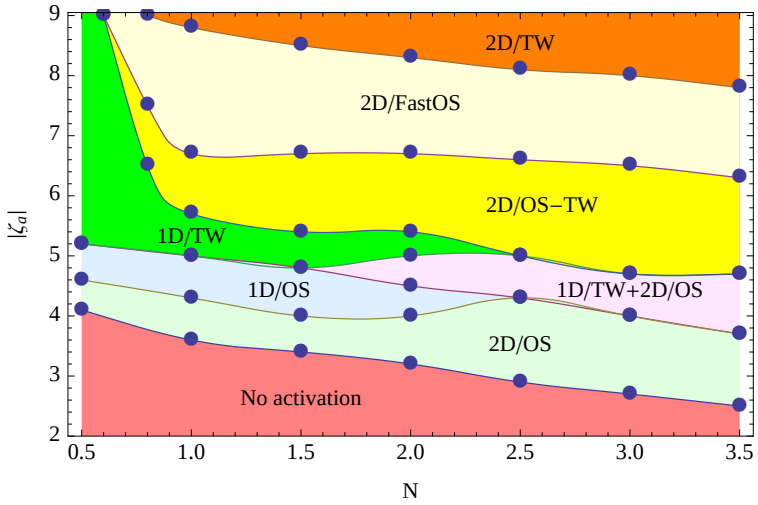

Figure 1: Active nematic phase diagram with induced polarity (without a polar interaction potential, $\alpha = \alpha_0 = 0$). The labels for each spatio-temporal attractor are given in Table 1 and described in the text.

1D/OS	1D banded oscillatory state
2D/OS	2D nonbanded oscillatory state
1D/TW	1D banded traveling waves
2D/OS-TW	2D traveling nonbanded oscillatory state
2D/TW	2D traveling nonbanded steady state
2D/FastOS	2D nonbanded with fast oscillations

Table 1: Notation for the observed long-lived attracting states.

We now summarize the key features of Figure 1.

First notice that the dependence on N is less sensitive than the dependence on ζ_a. Sitting at fixed N, vertical slices more or less pass through the same bifurcation sequence, summarized in Table 2.

$N < 0.6$	$0.6 < N < 1.5$	$1.5 < N < 2.5$	$2.5 < N < 3.5$
isotropic	isotropic	isotropic	isotropic
2D/OS	2D/OS	2D/OS	2D/OS
1D/OS	1D/OS	1D/OS	
		1D/TW+2D/OS	1D/TW+2D/OS
1D/TW	1D/TW	1D/TW	
	2D/OS-TW	2D/OS-TW	2D/OS-TW
	2D/FastOS	2D/FastOS	2D/FastOS
	2D/TW	2D/TW	2D/TW

Table 2: Bifurcation sequences versus activation parameter ζ_a for different intervals of nanorod volume fraction N. The top row is for sufficiently low ζ_a, with increasing ζ_a going down.

For a sufficiently small magnitude of ζ_a (in the region labeled "No activation" in Figure 1), the random initial perturbation of the isotropic equilibrium gradually dissipates, leaving no visible flow in the suspension with uniform nanorod concentration in the physical domain. We now list and describe the primary attractors in Figure 1.

2d oscillatory attractor, labelled 2D/OS, Figure 1. The critical activation value of $|\zeta_a|$, where the instability of the isotropic state begins to build up, decreases as the nematic strength N increases (as shown by the bottom curve in Figure 1). After the initial random perturbation is smoothed out, an unsteady 1d oscillatory structure with small amplitude is first observed. At long times, it then gradually transforms to a stable 2d oscillatory structure (in the region labeled "2D/OS"). This structure has been investigated carefully in our paper [10]. Figure 2 shows some snapshots of the final 2d oscillatory state for $N = 2$ and $\zeta_a = -3.4$. In the top-left figure, two elliptic points and two hyperbolic points are clearly seen in the streamlines of the velocity field. Local concentration attains its maximum at the hyperbolic points, and the minimum at the elliptic points. These flow stationary points disintegrate and reform with a period of about 1.98 time units. The polarity vector field in the middle column of Figure 2 strongly correlates with the flow field. Herring-bone patterns are observed in the nematic director field, column 3, with domains of nearly isotropic order along the ridges of the patterns. In the kinetic theory, there are two scalar order parameters associated with the two measures (polarity and nematic order) for mesoscopic orientation, $|\mathbf{n}|$ and the nematic order parameter s, the difference of the two leading eigenvalues of $\mathbf{M}$. When $|\mathbf{n}|$ is zero, the polarity vector is undefined. Likewise, when s is zero, the nematic director is undefined. So, we might well call the first case a defect associated with the polarity vector and the second case a nematic defect. Our results show the two defects are not necessarily correlated. In the middle column, we observe the evolution of pairs of degree ± 1 polarity defects, where they form in tandem vertically and

horizontally. In column 3, the nematic defect forms along a curve at some time and then breaks up into islands at other times. During the transition, nematic defects annihilate. In the nematic defect region, domain walls are apparent, either along disclination lines or the periphery of islands.

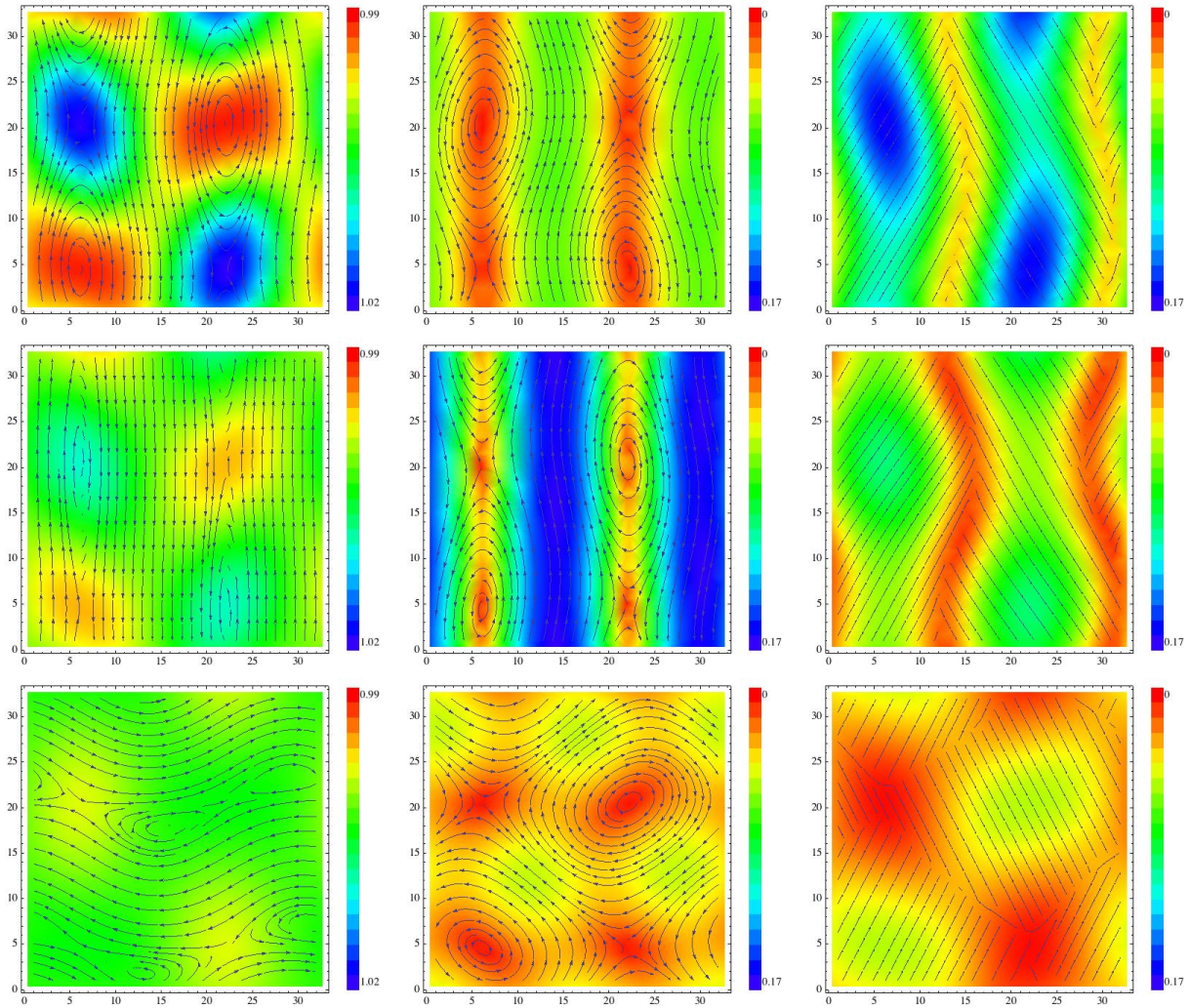

Figure 2: Snapshots of a 2D oscillatory attractor, labelled 2D/OS, for $N = 2, \zeta_a = 3.4$. Left column: Streamline of the velocity field with local concentration color-coded background. Middle column: Patterns formed by the polarity director superimposed with $|\mathbf{n}|$. Right column: Patterns formed by the nematic director with the order parameter s in background. Time: top row at $t = 242.56$, middle row at $t = 243.04$, and bottom row at $t = 243.52$.

1d banded oscillatory attractor, labelled 1D/OS. For $N < 2.5$, increasing the magnitude of ζ_a, the elliptic and hyperbolic regions in the stable 2D/OS state expand and then disappear, after which a stable oscillatory 1d banded structure emerges. This structure is also reported in [10], and not shown here in detail, but they are very similar to the top row snapshots of Figure 3. The salient features of this 1D/OS attractor are described in [10], with the distinctive feature of flow reversal

fluctuations with the shear bands.

1d steady and traveling banded attractors, labelled 1D/TW. For $N < 1.5$, with increasing $|\zeta_a|$, the 1d banded structure converges to a stationary steady state as reported in [10]. As $|\zeta_a|$ increases slightly, the stationary 1d banded structure develops a uniform translational velocity in the direction perpendicular to the uniform bands.

A hybrid 1d/2d attractor, switching between traveling 1D bands and a 2D oscillatory pattern, labelled 1D/TW + 2D/OS, Figure 3. For $N > 1.5$ and intermediate values of $|\zeta_a|$, a hybrid attractor emerges, switching between 1d bands that translate at uniform speed (top row, Figure 3) and a 2d stationary, oscillating structure (bottom row, Figure 3). As $|\zeta_a|$ increases, the duration of the 1D translating pattern drops while that of the 2d oscillating pattern grows. We calculate the spatial discrete Fourier transform of $f_0(\mathbf{x},t)$,

$$\begin{aligned} C_{m,n} &= \Sigma_{j=0}^{N_1-1}\Sigma_{k=0}^{N_2-1} c_{j,k}\cos\left(\frac{2\pi jm}{N_1}+\frac{2\pi kn}{N_2}\right), \qquad 0\le m<N_1, 0\le n<N_2 \\ S_{m,n} &= \Sigma_{j=0}^{N_1-1}\Sigma_{k=0}^{N_2-1} c_{j,k}\sin\left(\frac{2\pi jm}{N_1}+\frac{2\pi kn}{N_2}\right), \qquad 0\le m<N_1, 0\le n<N_2 \end{aligned} \tag{9}$$

where, $c_{j,k}$ are the discrete values of the local concentration $f_0(\mathbf{x},t)$ at the grid points. The magnitudes $\sqrt{C_{m,n}^2+S_{m,n}^2}$ of four representative Fourier modes are shown in Figure 4 for $0<t<1000$ when $N=2.5, |\zeta_a|=4.5$. In the (2,0) mode, the tilted line corresponds to the unsteady 1d, banded, traveling state, interrupted by short-lived 2d rapid oscillations. The 1d traveling wave dominates while the 2d oscillation occurs in a very short time. For all other Fourier modes, similar spikes in the Fourier amplitudes arise during the short-lived 2d phase. As $|\zeta_a|$ increases to around 5 for $N=2.5$, the 1d traveling wave disappears completely, giving way to a purely 2d oscillatory state.

2d traveling oscillatory state. For $N > 0.6$, the 1D/TW attractors destabilize with increasing $|\zeta_a|$, giving way to 2d patterns that oscillate (labelled 2D/OS), and at slightly higher values acquire an additional translation mode at a uniform speed (labelled 2D/OS-TW). Figure 5 gives snapshots of the latter attractors.

2d violent oscillatory state. The region in Figure 1 labelled " 2D/FastOS" refers to a rapidly oscillating 2D state with period much shorter than other 2d oscillatory states. Some snapshots are shown in Figure 6 for $N=2.5, \zeta_a=-6.7$, which has a period around 0.48 time units. Instead of two elliptic and two hyperbolic points located in the velocity field of the 2D/OS state in Figure 5, there are four elliptic and hyperbolic points in the velocity field in Figure 6 (left column), with similar features in the induced polarity vector (middle column) and the nematic director (right column).

Translational 2d structure. For sufficiently large $|\zeta_a|$, the 2d violent oscillation dies down to a small amplitude, uniformly translating 2d structure, labeled 2D/TW in Figure 1, for all dilute volume fractions $N > 0.6$. A snapshot for the steadily traveling 2d structure is given in Figure 7 (left) for $N=2.5, \zeta_a=-8.6$, where the velocity field $\mathbf{v}$ is superimposed with the local concentration f_0. The structure steadily travels toward the upper left. Unlike all states discussed above, two

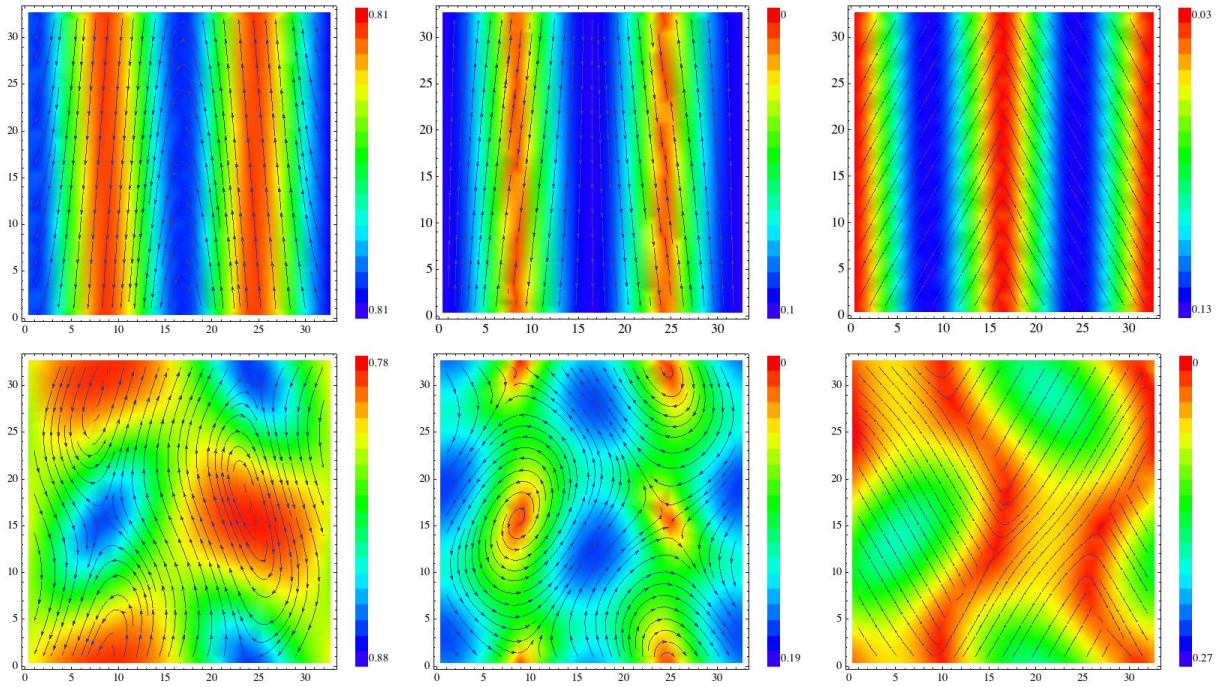

Figure 3: **Translational motion of the mesoscopic pattern (1D/TW+2D/OS).** Snapshots of the hybrid 1D/TW + 2D/OS attractor, consisting of a traveling 1D banded structure (top row) for some duration that switches back and forth between a 2D oscillating pattern. The values used here from Figure 1 are $N = 2.5, \zeta_a = 4.5$. Left column: Streamlines of the 1D velocity field with local nanorod concentration in the background. Middle column: Patterns formed by the induced polarity director superimposed with $|\mathbf{n}|$. Right column: Patterns formed by the nematic director with the order parameter s in the background.

Poiseuille-like velocity bands are clearly present in this structure, oriented in opposite directions. Figure 7 (middle) is a snapshot of the pattern formed by the polarity director, while Figure 7 (right) is a snapshot of the nematic pattern superimposed with the nematic order parameter.

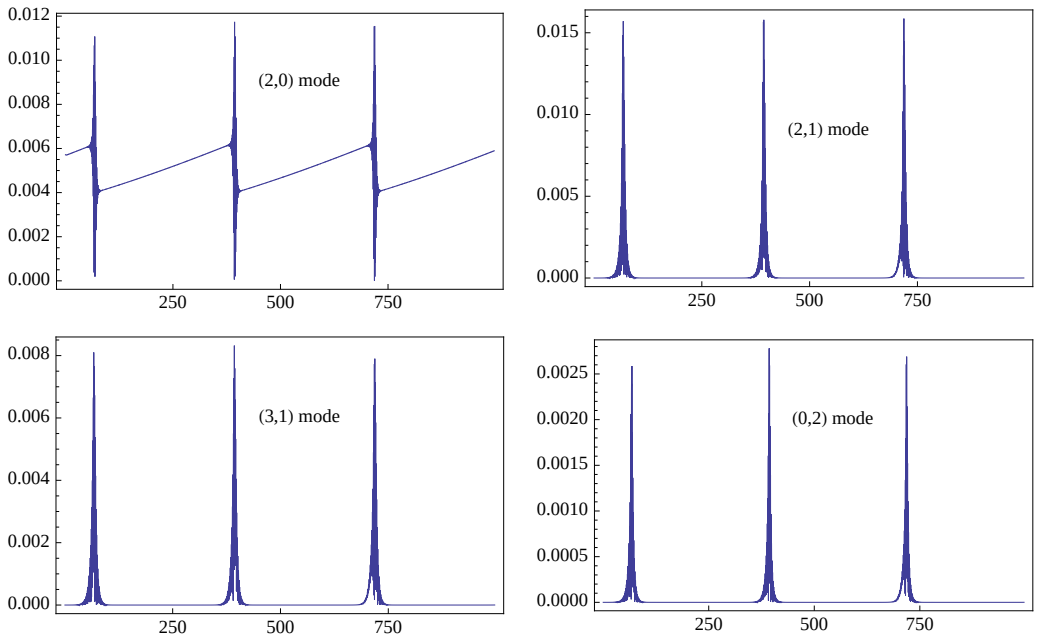

Figure 4: From the hybrid attractor of Figure 3, the time series of four spatial Fourier modes showing a slow growth during the 1D traveling wave phase and a short-lived rapid oscillation during the 2D oscillatory phase. Note the y-dependent Fourier modes vanish except during the brief 2D oscillations.

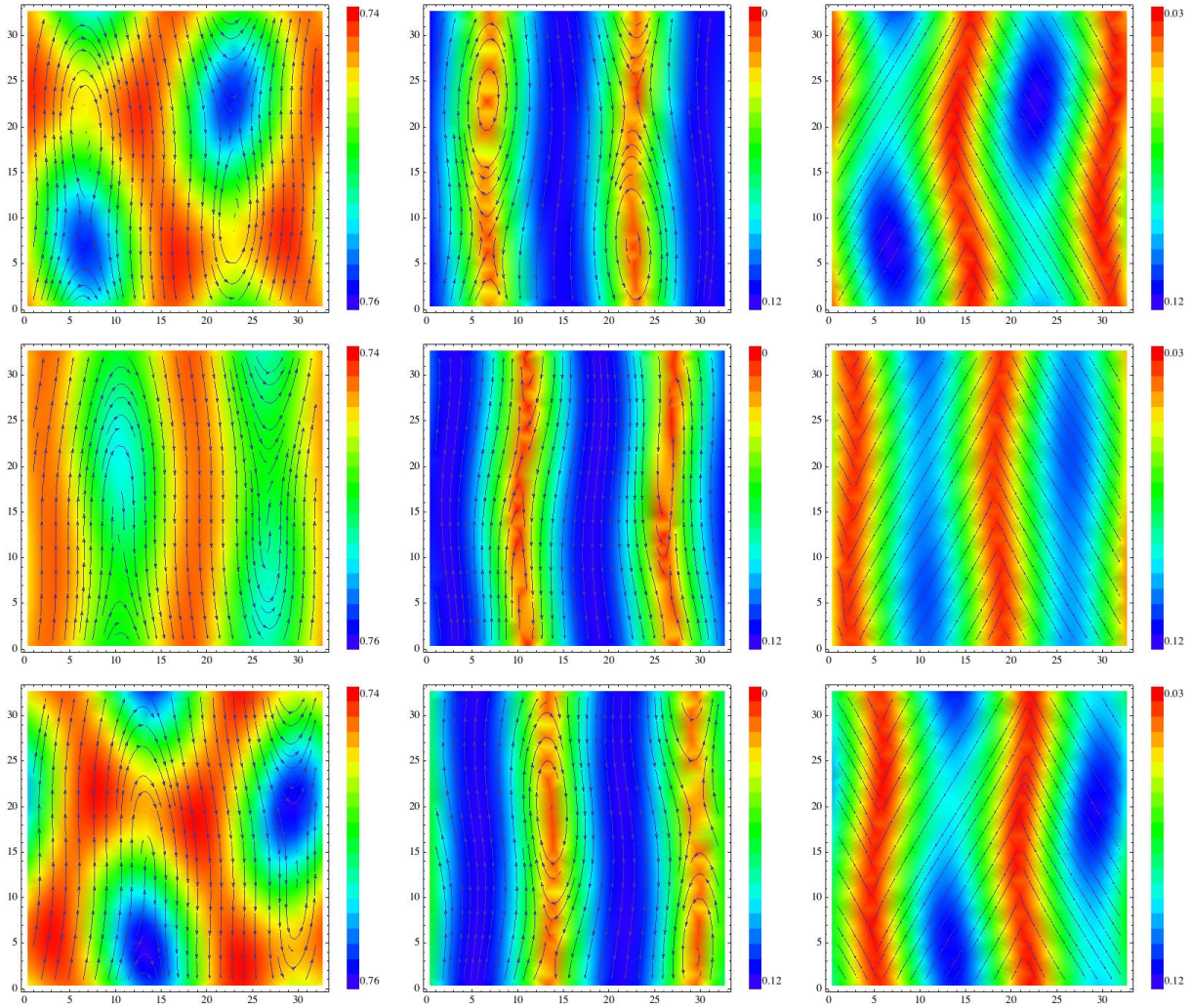

Figure 5: Snapshots of the 2D attractor that oscillates and translates, labelled 2D/OS-TW in Figure 1, for $N = 2, \zeta_a = -5.6$. Left column: Streamlines of velocity with local concentration in background. Middle column: Patterns formed by the induced polarity director superimposed with $|\mathbf{n}|$. Right column: Patterns formed by the nematic director with the order parameter s in the background. Snapshots are taken at time $t = 243.52$ (top row), $t = 244$ (middle row), and $t = 246.56$ (bottom row).

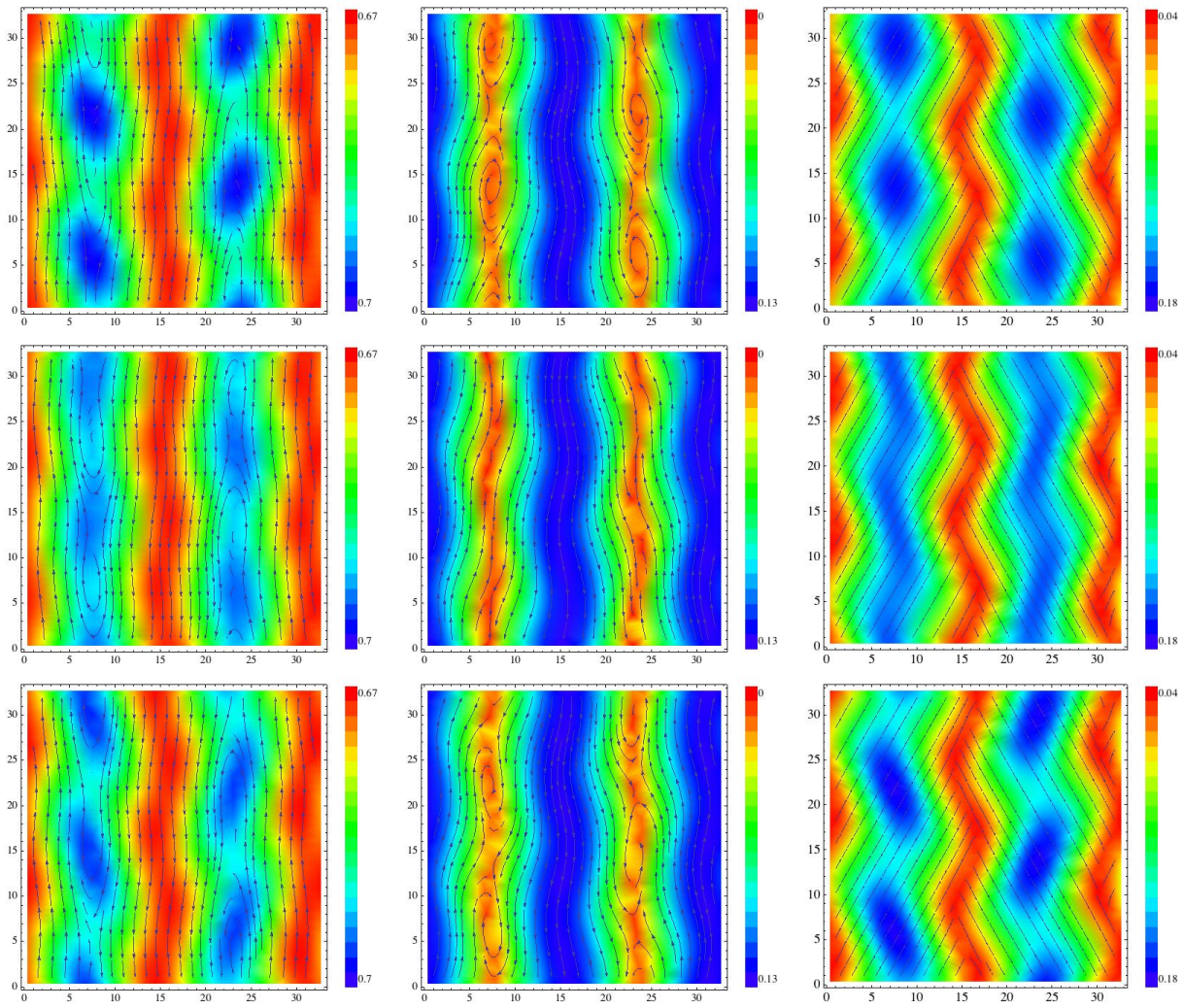

Figure 6: Snapshots of the attractor labelled 2D/FastOS in Figure 1, for $N = 2.5, \zeta_a = -6.7$. Left column: Streamlines of velocity with local concentration in background. Middle column: Patterns formed by the induced polarity director superimposed with $|\mathbf{n}|$. Right column: Patterns formed by the nematic director with the order parameter s in the background.

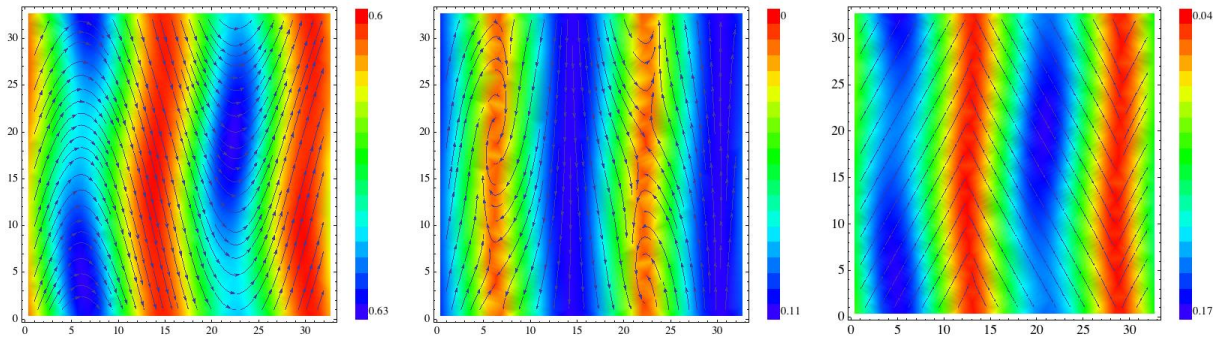

Figure 7: Snapshots of a traveling wave 2D structure (labelled 2DTW) for $N = 2.5, \zeta_a = -8.6$. Left: Streamlines of the velocity field with the local concentration in background. Middle: Patterns formed by the induced polarity director superimposed with $|\mathbf{n}|$. Right: Patterns formed by the nematic director with the order parameter s in the background.

2.2 Active polar nematic suspensions with a polar interaction potential

The phase diagram for active polar nematic suspensions with $\alpha = \alpha_0 = 1$ and all other parameters the same as in Figure 1, is given in Figure 8. The same labels are used for the various attractors since there are no new attractors. The effect of the polar interaction potential is similar to an increase in rod volume fraction, which is evident by comparison of Figures 1 and 8.

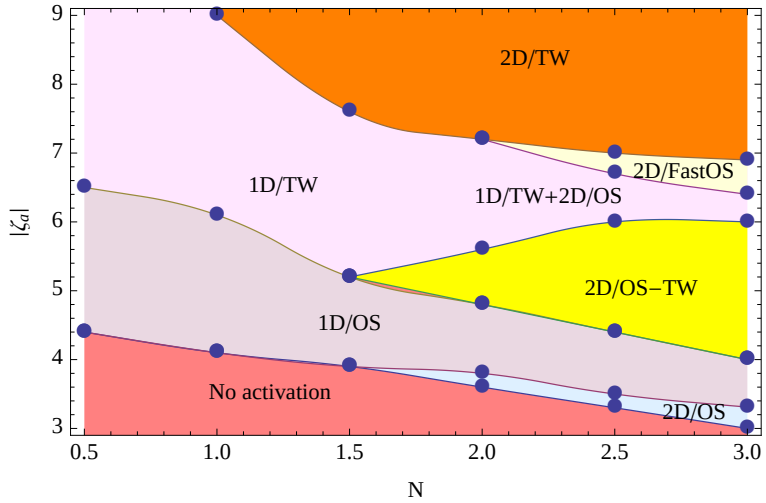

Figure 8: Phase diagram for polar active nematic suspensions with $\alpha = \alpha_0 = 1$. The labels for each attractor are explained in Table 1.

3 Conclusion

Phase diagrams of the spatio-temporal attractors of active nematic (nanorod) suspensions are presented both with and without first-order rod polarity. In all cases, particle activation induces polarity. These results are based on large-scale simulations of the kinetic-hydrodynamic theory of active nematic suspensions spanning nanorod volume fractions in the dilute regime and particle activation strength. Banded 1d and cellular 2d structures, some stationary, some stationary yet fluctuating, and others fluctuating and uniformly translating, are reported across the two-parameter phase diagrams. These results reproduce at dilute volume fractions all previously reported banded and 2D attractors from mesoscopic closure models of Landau-deGennes type of active nematics at nematic or semi-dilute concentrations [12, 13, 14, 15, 20, 21, 24, 25, 26, 28, 29, 34, 35, 36, 46]. Furthermore, new attractors are revealed, in particular those with a translational mode superimposed on unsteady banded and cellular patterns. Extensions of these kinetic-hydrodynamic results to higher volume fractions where the equilibrium nanorod dispersion is either bi-stable or nematic are in progress.

These are the most resolved simulations of the kinetic-hydrodynamic theory of polar active nematics, consisting of a coupled system of 125 nonlinear partial differential equations in 2 space dimensions and time with full orientational degrees of freedom. These space-time attractors undergo 1d to 2d spatial pattern transitions versus nanorod volume fraction, as well as dynamic transitions versus activity strength, including stationary to oscillatory standing wave patterns, periodic switching between 1d and 2d oscillating patterns, changes in oscillation frequencies of the spatial patterns and switching frequency, and onset of a traveling wave motion of all patterns at intermediate to high particle activation strengths.

Acknowledgements: This research is sponsored by the National Science Foundation grants DMS-1200487, DMS-1412844, and DMR-1122483, the Air Force Office of Scientific Research grant FA9550-12-1-0178, the Army Research Office grant 12-60317-MS, and the SC EPSCOR GEAR grant.

References

[1] B. Ermentrout, Simulating, Analyzing, and Animating Dynamical Systems: A Guide to Xpaut for Researchers and Students (Software, Environments, Tools), Society for Industrial and Applied Mathematics (2002).

[2] A. Baskaran and M. C. Marchetti, Nonequilibrium statistical mechanics of self propelled hard rods J. Stat. Mech. P04019 (2010).

[3] M. Doi and S.F. Edwards, **The Theory of Polymer Dynamics**. Oxford University Press (Clarendon), London New York (1986).

[4] E.J. Doedel, A.R. Champneys, T.F. Fairgrieve, Y.A. Kuznetsov, B. Sandstede, and X. Wang, AUTO97: continuation and bifurcation software for ordinary differential equations. Concordia University, (1997).

[5] M.G. Forest, Q. Wang, and X. Yang, LCP droplet dispersions: a two-phase, diffuse-interface kinetic theory and global droplet defect predictions, Soft Matter, 8, 9642-9660 (2012).

[6] M.G. Forest, R. Zhou, and Q. Wang, Explicit flow-aligned orientational distribution functions for dilute nematic polymers in weak shear, J. Non-Newt. Fluid Mech., 116(2-3), 183-204 (2004).

[7] M.G. Forest, Q. Wang, and R. Zhou, The weak shear phase diagram for nematic polymers, Rheol. Acta 43 (1), 17-37 (2004).

[8] M.G. Forest, Q. Wang, and R. Zhou, The flow-phase diagram of Doi-Hess theory for sheared nematic polymers II: finite shear rates, Rheol. Acta, 44 (1), 80-93 (2004).

[9] M.G. Forest, R. Zhou, and Q. Wang, Kinetic structure simulations of nematic polymers in plane Couette cells, II: In-plane structure transitions, SIAM Multiscale Model. Simul., 4(4), 1280-1304 (2005).

[10] M.G. Forest, Q. Wang, and R. Zhou, Kinetic Theory and Simulations of Active Nematic Polymers, Soft Matter, 9, 5207-5222 (2013).

[11] S. Furthauer, M. Neef, S. W. Grill, K. Kruse, and F. Julicher, The Taylor-Couette motor: Spontaneous flows of active polar fluids between two coaxial cylinders, New. J. Phys. 14, 023001 (2012).

[12] F. Ginelli, F. Peruani, M. Bar, and H. Chate, Large-scale collective properties of self-propelled rods, Phys. Rev. Lett. 104, 184502 (2010).

[13] L. Giomi, M.C. Marchetti, and T.B. Liverpool, Complex spontaneous flows and concentration banding in active polar films, Phys. Rev. Lett. 101, 198101 (2008).

[14] L. Giomi, L. Mahadevan, B. Chakraborty, and M. F. Hagan, Excitable patterns in active nematics, Phys. Rev. Lett. 106, 218101 (2011).

[15] L. Giomi and M. C. Marchetti, Polar patterns in active fluids, Soft Matter, 8, 129 (2012).

[16] S. Hess, Fokker-Planck-equation approach to flow alignment in liquid crystals, Z. Naturforsch Teil, 31A, 1034 (1976).

[17] C. Hohenegger and M. Shelley, Stability of active suspensions, Phys. Rev. E 81, 046311 (2010).

[18] T. Ishikawa, J.T. Locsei, and T.J. Pedley, Development of coherent structures in concentrated suspensions of swimming model micro-organisms. J. Fluid Mech. 615, 401-431 (2008).

[19] F.C. Keber, E. Loiseau, T. Sanchez, S.J. DeCamp, L. Giomi, M.J. Bowick, M.C. Marchetti, Z. Dogic, and A.R. Bausch, Topology and dynamics of active nematic vesicles, Science, 345 (6201), 1135-1139 (2014).

[20] D. Koch and G. Subramanian, Collective hydrodynamics of swimming micro-organisms: living fluids, Annu. Rev. Fluid Mech., 43, 637-659 (2011).

[21] W. Kung, M.C. Marchetti, and K. Saunders, Hydrodynamics of polar liquid crystals, Phys. Rev. E, 73, 031708 (2006).

[22] R. G. Larson and H. C. Ottinger Effect of molecular elasticity on out-of-plane orientations in shearing flows of liquid-crystalline polymers Macromolecules, 24, 6270-6282 (1991).

[23] T. B. Liverpool and M. C. Marchetti, Hydrodynamics and rheology of active polar filaments, in Cell Motility, P. Lenz editor (Springer, New York, 2007).

[24] M.C. Marchetti, J.F. Joanny, S. Ramaswamy, T.B. Liverpool, J. Prost, M. Rao, and R. A. Simha, Hydrodynamics of soft active matter, Rev. Modern Phys., 85, 1143-1190 (2013).

[25] D. Marenduzzo, E. Orlandini, and J.M. Yeomans, Hydrodynamics and rheology of active liquid crystals: A numerical investigation, Phys. Rev. Lett. 98, 118102 (2007).

[26] D. Marenduzzo, E. Orlandini, M.E. Cates, and J.M. Yeomans, Steady-state hydrodynamic instabilities of active liquid crystals: Hybrid lattice Boltzmann simulations, Phys. Rev. E 76, 031921 (2007).

[27] G. Marrucci and F. Greco, Flow behavior of liquid crystalline polymers, Adv. Chem. Phys., 86, 331-404 (1993).

[28] M.E. Cates, S.M. Fielding, D. Marenduzzo, E. Orlandini, and J.M. Yeomans, Shearing active gels close to the isotropic-nematic transition, PRL 101, 068102 (2008).

[29] S. Mishra, A. Baskaran, and M.C. Marchetti, Fluctuations and pattern formation in self-propelled particles, Phys. Rev. E 81, 061916 (2010).

[30] A.R. Morgan, A.B. Dawson, H.S. Mckenzie, T.S. Skelhon, R. Beanland, H.P.W. Franks, and S.A.F. Bon, Chemotaxis of catalytic silicamanganese oxide matchstick particles, Materials Horizons, 1, 65-68 (2014).

[31] A.A. Pahlavan and D. Saintillan, Instability regimes in flowing suspensions of swimming micro-organisms, Phys. Fluids, 23, 011901 (2011).

[32] J. Palacci, S. Sacanna, S.H. Kim, G.R. Yi, D.J. Pine, and P.M. Chaikin, Light-activated self-propelled colloids, Philosophical Transactions A, 372, 2029 (2014).

[33] W.F. Paxton, K.C. Kistler, C.C. Olmeda, A. Sen, S.K. St Angelo, Y.Y. Cao, T.E. Mallouk, P.E. Lammert, and V.H. Crespi, Catalytic nanomotors: autonomous movement of striped nanorods. J. Am. Chem. Soc. 126, 1342413431 (2004).

[34] D. Saintillan and M.J. Shelley, Orientational order and instabilities in suspensions of self-locomoting rods, Phys. Rev. Lett. 99, 058102 (2007).

[35] D. Saintillan and M.J. Shelley, Instabilities and pattern formation in active particle suspensions: kinetic theory and continuum simulations, Phys. Rev. Lett. 100, 178103 (2008).

[36] D. Saintillan and M.J. Shelley, Instabilities, pattern formation, and mixing in active suspensions, Phys. Fluids 20, 123304 (2008).

[37] D. Saintillan, Extensional rheology of active suspensions, Phys. Rev. E 81, 056307 (2010).

[38] D. Saintillan, The dilute rheology of swimming suspensions, a simple kinetic model, Exp. Mech. 50, 1275-1281 (2010).

[39] D. Saintillan and M. Shelley, Active Suspensions and Their Nonlinear Models, Comptes Rendes Physique 14, 497-517 (2013).

[40] B. Ezhilan, M. J. Shelley, and D. Saintillan Instabilities and nonlinear dynamics of concentrated active suspensions, Physics of Fluids 25, 070607 (2013).

[41] V. Schaller, C. Weber, C. Semmrich, E. Frey and A. R. Bausch, Polar patterns of driven filaments, Nature, 467, 7377 (2010).

[42] A. Sokolov and I. S. Aranson, Reduction of viscosity in suspension of swimming bacteria, Phys. Rev. Lett. 103, 148101 (2009).

[43] A. Sokolov, I. S. Aranson, J.O. Kessler and E. Goldstein, Concentration dependence of the collective dynamics of swimming bacteria, Phys. Rev. Lett. 98, 158102 (2007).

[44] T. Tsuji and A.D. Rey, Effect of long range order on sheared liquid crystalline polymers, part 1 compatibility between tumbling behavior and fixed anchoring, J. Non-Newt. Fluid Mech., 73, 127-152 (1997).

[45] R. Voituriez, J.F. Joanny, and J. Prost, Spontaneous flow transition in active polar gels, Europhys. Lett. 70, 404 (2005).

[46] R. Voituriez, J. F. Joanny, and J. Prost, Generic phase diagram of active polar films, Phys. Rev. Lett. 96, 028102 (2006).

[47] W. Wang, W. Duan, S. Ahmed, T.E. Mallouk, and A. Sen, Small power: autonomous nano- and micromotors propelled by self-generated gradients. Nano Today 8, 531554 (2013).

[48] X. Yang, M. G. Forest, W. Mullins, and Qi Wang, Dynamic defect morphology and hydrodynamics of sheared nematic polymers in two space dimensions, J. Rheology, 53(3), 589-615 (2009).

[49] X. Yang, Q. Wang, W. Mullins, and M.G Forest, 2D lid-driven cavity flow of nematic polymers: an unsteady sea of defects, Soft Matter, 6, 1138-1156 (2010).